



H₂ oxidation on doped yttrium chromites/yttrium stabilized zirconia anode of solid oxide fuel cell



Wenyuan Li, Mingyang Gong, Xingbo Liu*

Mechanical and Aerospace Engineering Department, West Virginia University, Morgantown, WV 26505, USA

HIGHLIGHTS

- H₂ oxidation mechanisms on Co and Ni doped yttrium chromites were investigated.
- Charge transfer process at HF and surface adsorption/diffusion processes at LF can be the dominant anode reaction steps.
- Reaction order is 1/4 for Co doped and 1/3–1/2 for Ni doped yttrium chromites.

ARTICLE INFO

Article history:

Received 15 March 2013

Received in revised form

18 April 2013

Accepted 21 April 2013

Available online 30 April 2013

Keywords:

SOFC

Ceramic anode

H₂ oxidation mechanisms

impedance

ABSTRACT

Co and Ni doped yttrium chromites as potential anodes for solid oxide fuel cell (SOFC) are studied with respect to the electrode performance and anode reaction mechanisms. Both electrical conductivity and electrode performance of yttrium chromites have been enhanced after Co and Ni doping. Electrochemical impedance spectroscopy (EIS) results indicate that charge transfer process at high frequency and surface adsorption/diffusion processes at low frequency domain can be the dominant anode reaction steps. Ni doping accelerates the surface processes by reducing the related activation energy from 1.2 to 0.5 eV. It also substantially improves the charge transfer process probably by increasing the amount of adsorbed H on electrode surface. The resistance of high frequency is found to be dependent on H₂ content. The observed reaction order is 1/4 for Co doped and 1/3–1/2 for Ni doped yttrium chromites. A model of H₂ oxidation reaction is proposed, revealing this dependence stems from the reaction between adsorbed H and the lattice oxygen.

© 2013 Elsevier B.V. All rights reserved.

1. Introduction

Ni/YSZ cermet is the most commonly used anode in SOFC with H₂ fed as fuel, but it would degrade in hydrocarbon and impurity containing syngas due to coking and poisoning by contaminants such as S [1]. Therefore, alternative materials are long desired to overcome these drawbacks of Ni/YSZ anode. Perovskite oxides such as doped lanthanum chromites [2–5] and lanthanum doped strontium titanate, etc. have been investigated extensively as potential anode materials [6–9]. The ABO₃ formula allows not only wide size variety at A and B sites but also different valence combination, making the electrical and catalytic properties adjustable [10]. YCrO₃ perovskite has been examined as possible interconnect material as they display advantages over the traditional LaCrO₃ based materials in terms of the

chemical expansion and compatibility with yttrium stabilized zirconia (YSZ) electrolyte [11–17]. In addition of working as interconnect, YCrO₃ based materials have been evaluated as potential anode after multiple doping at A and B sites: an anode made from Ca and Co doped YCrO₃ lately has demonstrated an encouraging performance in H₂, and more importantly, displayed good tolerance towards 20 ppm H₂S [18]. However to our best knowledge, besides the electrode performance research, no investigation regarding the anode reaction mechanism on YCrO₃ based materials has been reported. Understanding on electrode reaction mechanism is important for the tailoring of material to further optimize electrode performance. In fact, on Pt and Ni-based anodes, mechanism and kinetics studies have been extensively investigated [19–27]. In these publications, it is generally recognized that most electrochemical reaction takes place at three-phase boundary (3PB) area and that the electrode performance is heavily dependent on the microstructure and electrode composition [25,28]. It is also known from the EIS studies that the

* Corresponding author.

E-mail address: xingbo.liu@mail.wvu.edu (X. Liu).

charge transfer process is relatively fast as compared to the adsorption and diffusion processes [29–31]. On the other hand, due to the variation on raw materials, electrode composition, manufacturing conditions and etc., different conclusions concerning reaction path and rate-limiting steps are also drawn out by different groups. These existent observations from Ni-based anodes could be relevant to the study of YCrO_3 based anodes as well.

In this work, in order to gain knowledge of anode reaction on YCrO_3 materials and evaluate electrode performance, Co and Ni doped YCrO_3 –YSZ composite anodes were developed and tested in H_2 -containing atmospheres by EIS. The effect of doping on catalytic activity and anode performance was evaluated. The rate-limiting steps and H_2 dependence of polarization resistance associated with different dopants were determined. At last a model concerning anode reaction mechanism was proposed based on these results.

2. Experiment

$\text{Y}_{0.8}\text{Ca}_{0.2}\text{CrO}_3$, $\text{Y}_{0.8}\text{Ca}_{0.2}\text{Cr}_{0.8}\text{Co}_{0.2}\text{O}_3$, $\text{Y}_{0.8}\text{Ca}_{0.2}\text{Cr}_{0.9}\text{Ni}_{0.1}\text{O}_3$, denoted as YCC, YCCC and YCCN respectively, were synthesized by EDTA–citric sol–gel method [32,33]. Standard nitrates (Alfa Aesar) in stoichiometric percentage together with citric acid (Alfa Aesar) were dissolved into distilled water. EDTA powders (Fisher Scientific) as complexant along with ammonia water (Alfa Aesar) was dissolved into the other set of distilled water. The above solutions were blended together followed by adjusting pH to 8 through ammonia water, then held at $\sim 80^\circ\text{C}$ and stirred until gelation. The gel was heated to 400°C to decompose nitrates and organic residual. Resultant powders were calcined at different temperatures for several cycles with intermediate ground to crystallize. Afterward, X-ray diffraction (XRD, PANalytical X'pert PRO and Bruker AXS, Cu $K\alpha$ radiation) test was conducted to examine purity of phase. Commercial software Jade 5 was used to analyze XRD spectra. Powders were also pressed into pellet for scanning electron microscopy (SEM, JEOL JSM-7600F) observation.

The calcined powders were pressed into pellet for DC conductivity testing. Each piece of 0.6 g powders was pressed into a pellet with 13 mm diameter and ~ 1 mm thickness under 220 MPa. These pellets were then sintered at 1200 – 1300°C for 4 h. The porosity of each sample was determined by Archimedes method (scale from Voyager Pro, model VP214CN). DC conductivity of the samples was measured using van der Pauw method with Au probes in ambient air at temperatures from 600 to 850°C [34,35].

To make anode slurry, these powders calcined at 1200°C were mixed with YSZ (TOSOH, 8% Y_2O_3 stabilized) and ground in ink vehicle (Fuel Cell Materials Co.). The weight ratio of anode powders: YSZ: vehicle was 4:6:11. Anode slurry was screen printed onto both sides of YSZ electrolyte symmetrically. The circular YSZ electrolyte (Nextech Co.) used as cell support was 28 mm in diameter and $\sim 350\ \mu\text{m}$ in thickness. The number of screen printing cycles depended on the designed electrode thickness. Typically, a single printing resulted in $5\ \mu\text{m}$ in thickness after sintering. The effect electrode area was $0.7\ \text{cm}^2$ at each side. The as-made symmetric cells were sintered at 1000°C for 2 h in air. Pt mesh was bonded to both electrodes as current collector using Pt paste, followed by heating at 700°C .

EIS testing was carried out on these symmetric cells in various H_2 -containing atmospheres by Solartron 1287 electrochemical interface and 1260 impedance analyzer at open circuit condition over frequency range from 0.1 Hz to 99 MHz. The AC signal applied was 20 mV. H_2 content in H_2/N_2 mixture was adjusted by mass flow controller (Alicat Scientific). H_2 -containing gases were all moisturized by passing through a water bubbler at room temperature before feeding to samples. The resultant spectra were deconvoluted using Z-view software.

3. Results

3.1. XRD patterns and SEM observation

Fig. 1 shows the XRD spectra from the powder samples of pristine and doped YCCs. All patterns except the one for YCCC calcined at 1100°C are single phase, showing the orthorhombic perovskite structure (PDF#48-0474). For YCCC treated at 1100°C , a foreign peak marked with a triangle at around 24.6° was detected and identified as the main peak of $\text{Ca}_2\text{Cr}_2\text{O}_5$ (PDF#48-0791) by Jade 5.0.

It has been reported by K.J. Yoon, etc. that pure phase Ca and Co co-doped YCrO_3 was obtained by glycine–nitrate method at 1200°C [18]. And they also confirmed good chemical stability of such material in oxidizing and reducing atmosphere and good compatibility with YSZ. But in our study, it was observed that diffusion between YCCC pellet and YSZ felt holder occurred when sintered above 1200°C . The investigation of sintering behavior of Ca–Cr system has been conducted in lots of literature [36,37]. As studied in the CaO – Cr_2O_3 phase system, liquid phase would appear when heating up to $\sim 1022^\circ\text{C}$ [38]. Doping Ca into Cr-based perovskite is employed to improve the sinterability because the transient liquid phase [39]. CaCrO_4 , $\text{Ca}_3(\text{CrO}_4)_2$, $\text{Ca}_5(\text{CrO}_4)_3$, etc., appear at different sintering phrases, and will eventually dissolve into the lattice when elevated temperature along with prolonged sintering time is used. What's more, Co is found to be able to complicate the transition of transient liquid phase further. Doping Co into $(\text{LaCa})(\text{CrCo})\text{O}_3$ facilitates the formation of liquid phase, resulting in an above 94% sinterability [40]. Indeed, it was found herein that YCCC sample experienced a liquid sintering phrase in the middle of sintering process. Some area on the surface of YCCC pellet sintered at 1100°C was coated by a glass-like phase, which can be seen by bare eye and also observed by SEM as shown in Fig 2(a). Such phenomenon has not been observed on YCC or YCCN. The shrinkage simply calculated from the sizes of sample before and after sintering at 1400°C is 17% for YCCC, compared to 15% for YCC and 12% for YCCN. Based on the facts above, it seems clear that Co doping facilitates the formation of Ca–Cr liquid phase, further improving the sinterability of yttrium chromites, even though Co itself somehow has not been significantly involved into this phase. EDS result for this glass-like phase shows the ratio of Y:Ca:Cr:Co is 0.1:1:1.1:0.03, in which the Ca:Cr ratio is consistent with the

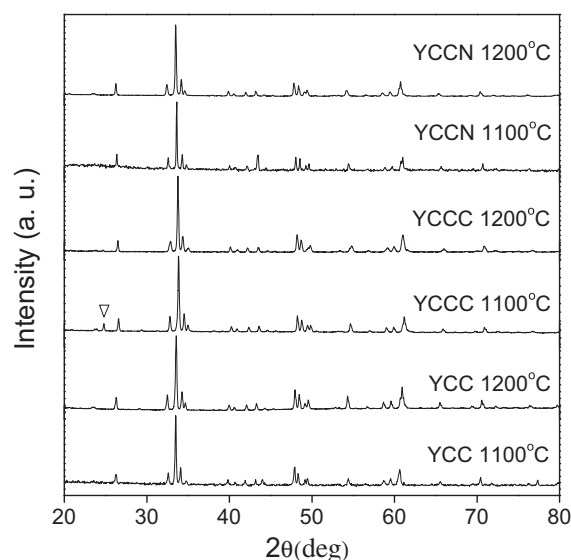


Fig. 1. XRD spectra of doped YCCs.

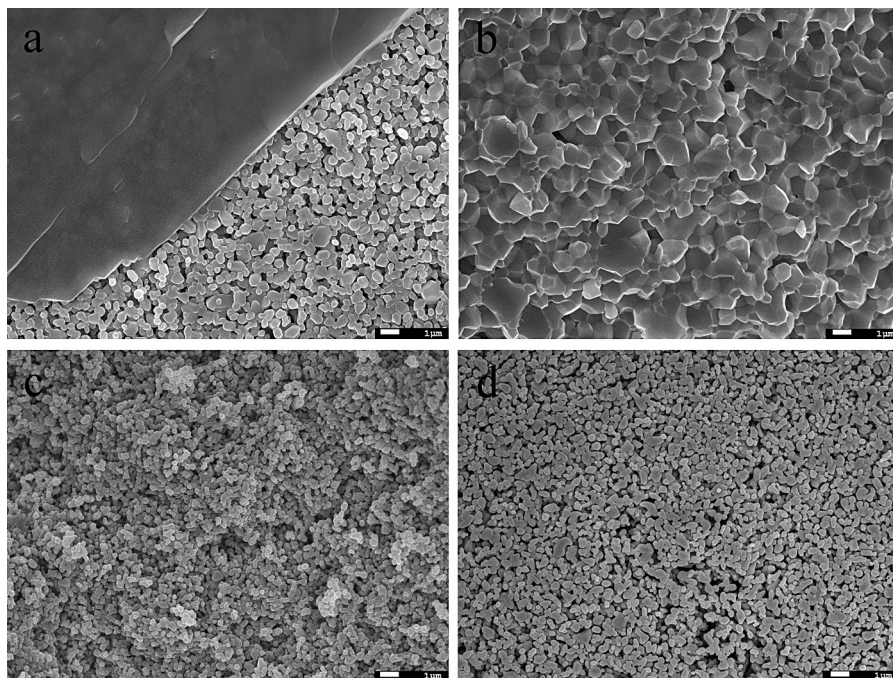


Fig. 2. Morphology of YCCC sintered at 1100 °C (a), 1200 °C (b), YCC (c) and YCCN (d) sintered at 1200 °C.

secondary phase $\text{Ca}_2\text{Cr}_2\text{O}_5$ identified by XRD at 1100 °C. The glass-like phase in YCCC disappeared as shown in Fig. 2 (b) when calcined at 1200 °C. Accordingly, only a tiny peak at 24.6° is detected by the XRD for 1200 °C calcined YCCC powder. Another consequence of Co facilitating sintering is that the particle size of YCCC is larger than those of YCC and YCCN sintered at the same temperature. As can be seen in Fig. 2, the grain size is 0.2–0.5 μm for YCC, 1–1.5 μm for YCCC and 0.2–0.5 μm for YCCN, respectively.

3.2. Electrical conductivities

Fig. 3a shows the electrical conductivities of YCCs in air. YCC, YCCC and YCCN pellets were sintered in air at 1300 °C, 1200 °C, 1300 °C, respectively, resulting in 93%, 98%, and 86% relative density. The data have been calibrated in terms of the porosity impact in a sphere sample [41]. Both conductivities of YCCC and YCCN increased upon doping, but the increase was much more pronounced for the former. The conductivity value reads 25, 44 and 28 S cm^{-1} for YCC, YCCC and YCCN at 850 °C, respectively. The value of YCCC is comparable with published results, while for YCC, it almost doubles [13]. The corresponding Arrhenius curves are plotted in Fig. 3b. Activation energy abstracted from the slope of each curve for YCC, YCCC and YCCN is 0.18, 0.25 and 0.19 eV, respectively, which is in consistency with the reported data in Ref. [11].

3.3. EIS results of YCCs in wet 5% H_2 – N_2

Fig. 4a shows the EIS for YCCN tested at 750 °C in wet 5% H_2 – N_2 (5% H_2 and 95% N_2). The solid lines are fitting arcs from Z-view program. Fig. 4b is the equivalent circuit used to fit that spectrum, where L represents the overall inductor from leading wires and Solartron eternal circuit, R_0 the total ohmic resistance composed of contributions from electrolyte, electrodes and leading wires. Constant phase element (CPE) is adopted due to the frequency dispersion phenomenon in electrode process [42].

As can be seen in Fig. 4a, the chosen equivalent circuit demonstrated a good representation of observed results. Four arcs in Fig. 4a imply at least four electrode processes are involved in H_2 oxidation reaction at this given condition. But as temperature and atmosphere vary, each arc will evolve in its own way according mainly to its activation energy.

By definition,

$$Y_{\text{CPE}} = Q^0(j\omega)^n, \quad (1)$$

where Q is the numerical value of admittance of Y_{CPE} , j the imaginary unit and ω the angular frequency, $\omega = 2\pi f$.

From fitting results, the characteristic frequency of each ($R_i\text{CPE}_i$) can be derived from Eq. (2) [43],

$$f_0 = \frac{1}{2\pi\sqrt[n]{RQ^0}} \quad (2)$$

The capacitance for ($R_i\text{CPE}_i$) coupled with certain electrode process can be computed by Eq. (3) [44],

$$C = Q^0(2\omega)^{n-1} \sin \frac{\pi n}{2} \quad (3)$$

Table 1 summarizes the resistance (R), capacitance (C), activation energy (E_a) and characteristic frequency (f_0) from EIS collected in wet 5% H_2 at 850 °C. In particular, Fig. 5 displays EIS for YCCs in wet 5% H_2 – N_2 at 850 °C tested at open circuit condition. The electrode thickness of all samples was $\sim 15 \mu\text{m}$. The polarization resistance, i.e. the difference between high and low frequency intercepts at real axis, is 235, 86 and 51 Ωcm^2 for YCC, YCCC and YCCN, respectively, and meanwhile all these spectra possess roughly similar shape, indicating that after doping the performance of YCC has been enhanced significantly but the main electrode processes remain the same. At this temperature two arcs, arc II and IV as shown in Fig. 4a, are dominant, denoted as high frequency (HF) arc and low frequency (LF) arc separately.

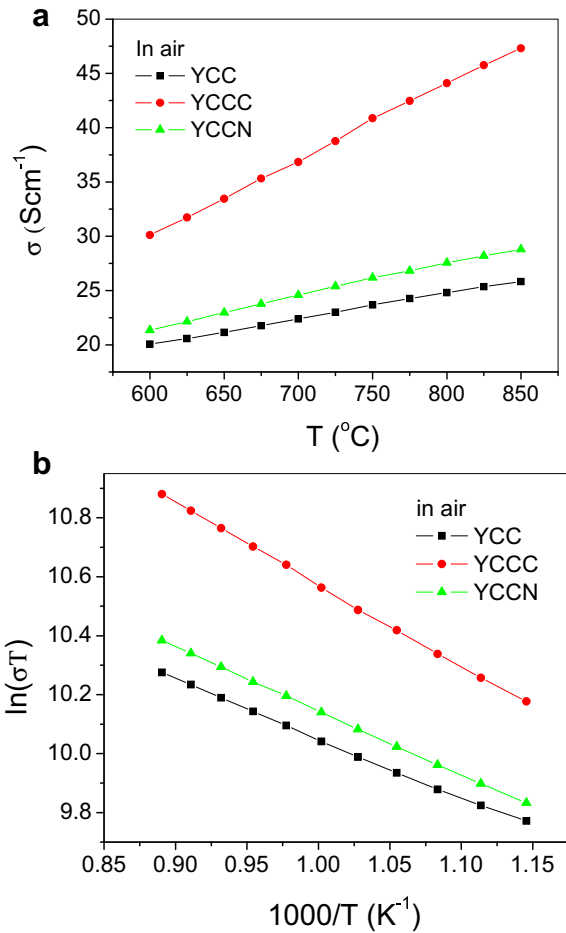


Fig. 3. a. Electrical conductivities of YCCs in air. b. Arrhenius curves for YCCs tested in air.

Fig. 6 demonstrates the Arrhenius curves for HF arc derived from EIS of YCCs in 5% wet H₂. Fairly good linearity in each curve implies either the HF is related with a single electrode process alone or one single process is strongly predominant among all the processes involved in HF range. Resistances from different samples can be ranked in order $R_{YCC} > R_{YCCC} > R_{YCCN}$ in the operating temperature range. The apparent activation energy (E_a) derived from Fig. 6 is

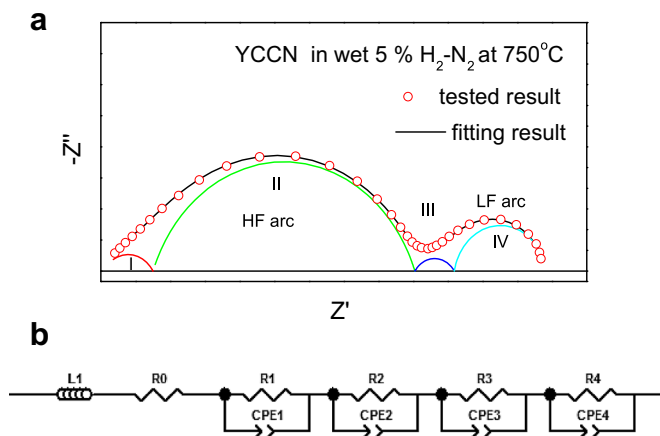


Fig. 4. a. Impedance of YCCN at 750 °C in wet 5% H₂-N₂ and the related fitting arcs. b. Equivalent circuit used to fit EIS.

Table 1

Summary of resistance (R), capacitance (C), activation energy (E_a) and characteristic frequency (f_0) for YCCs tested in wet 5% H₂-N₂ at 850 °C.

In wet 5% H ₂ -N ₂ at 850 °C		R (Ω cm ²)	C (F cm ⁻²)	E_a (eV)	f_0 (Hz)
HF arc	YCC	157	2.0×10^{-7}	1.2	4800
	YCCC	44	1.4×10^{-7}	1.2	25000
	YCCN	24	2.3×10^{-7}	1.3	27000
LF arc	YCC	43	0.7×10^{-3}	1.2	1
	YCCC	26	1.6×10^{-3}	1.0	4
	YCCN	18	3.8×10^{-3}	0.5	2

almost invariant, with values of 1.2, 1.3 and 1.2 eV for YCC, YCCC and YCCN, respectively. The data at 650 °C seem to deviate from the trends for other temperatures for all three types of materials, indicating that the predominating processes for these materials may transit to different ones at lower temperatures.

Fig. 7 shows the corresponding capacitance for HF arcs in wet 5% H₂ calculated from Eq. (3). All of the capacitance for YCCs approximately keeps unchanged at different temperatures. This trend is in consistent with that reported for the double layer capacitance of Ni/YSZ anode by Primdahl and Mogensen [22].

3.4. EIS results of YCCs in wet H₂-N₂ with various H₂ partial pressures

Fig. 8 displays the impedance of YCCN in wet H₂-N₂ with various H₂ partial pressures under open circuit condition at 850 °C. The electrode thickness of this YCCN symmetrical cell is about 40 μ m. EIS testing was carried out in H₂ partial pressure range from $10^{-1.5}$ to 1 atm by the increment of $10^{0.25}$ atm. Only one arc was observed in each spectrum in Fig. 8, except a very small distorted tail appearing at low frequency under very low P_{H_2} . In contrast, the spectrum of cell with 15 μ m thick electrode rather consists of two arcs in Fig. 5 where P_{H_2} is 0.5 atm. It has been reported that EIS spectra can be highly sensitive to microstructure and thickness of the SOFC electrodes. Jorgensen reported two EIS spectra different in magnitude and profile were obtained from LSM/YSZ cathodes in 4 and 6 μ m thickness, respectively, due to variation in the microstructure and composition [45]. Brown addressed in detail the influence of microstructure on EIS using a range of Ni/YSZ anode made out of different manufacturing conditions and raw materials [46]. In particular, an active thickness of 10 μ m was demonstrated in their work based on the ionic conductivity of YSZ in the cermet structure. The electrode impedance changed significantly over this threshold. Besides these observations above, for YCCN electrode, another factor might also account for the variation of spectra upon change in electrode thickness. Compared to Ni/YSZ or even to LSM/YSZ electrode, the electronic conductivity of YCCN-YSZ composite electrode is 2–3 orders lower. Poor conductivity of such electrode would certainly increase ohmic loss. But it may also lower the

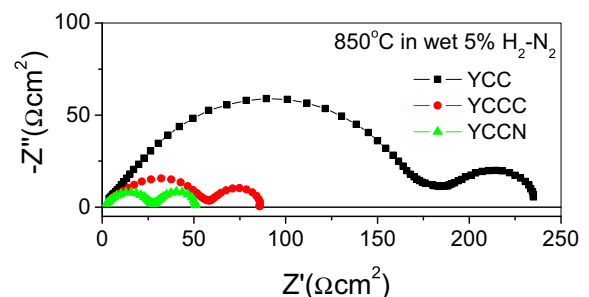


Fig. 5. Impedance of YCCs at open circuit condition tested in wet 5% H₂-N₂ at 850 °C.

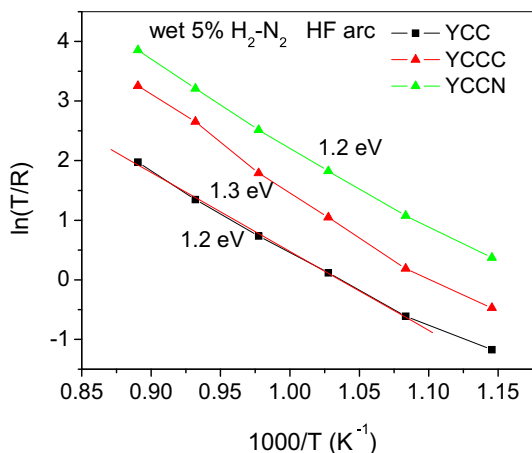


Fig. 6. Arrhenius curves for HF arc derived from EIS of YCCs in wet 5% $\text{H}_2\text{-N}_2$ from 600 to 850 °C.

kinetics of electrode reactions involving electron, even though the resistivity of electron transportation will not be taken into account when dealing with kinetic reactions in electrodes with high electronic conductivity. In this case, the polarization resistance could be sensitive to the thickness of electrode. It becomes relatively harder to remove electrons created by electrode reaction as YCCN–YSZ anode turns thicker. f_0 for this arc enlarged from 4000 to 20,000 Hz as increasing H_2 content, which can be denoted as HF one. Resistance for this HF arc increased as lowering P_{H_2} .

Fig. 9 shows the temperature dependence of resistance and capacitance for the HF arc of YCCN sample when operated at $\log(P_{\text{H}_2}/\text{atm}) = 0$ and -1.5 . Over the operating temperature range, capacitances in both conditions tend to remain unchanged, and have the same scale as HF arcs in YCCs in Fig. 7.

Arrhenius curves for HF arc of this sample are plotted in Fig. 10. The curve under each P_{H_2} shows good linearity. E_a is the same, 1.2–1.3 eV, regardless of H_2 content.

The double logarithm plot in Fig. 11 shows the H_2 dependence of HF arc in different temperature. The reaction order n in the relationship of $1/R \propto P_{\text{H}_2}^n$ is the slope of each curve, ranging from 1/3 to 1/2 as marked in Fig. 11.

In short, the main results of this present study can be summarized as following:

- Both Co and Ni doping at B site enhanced the electronic conductivity and catalytic performance of YCC.

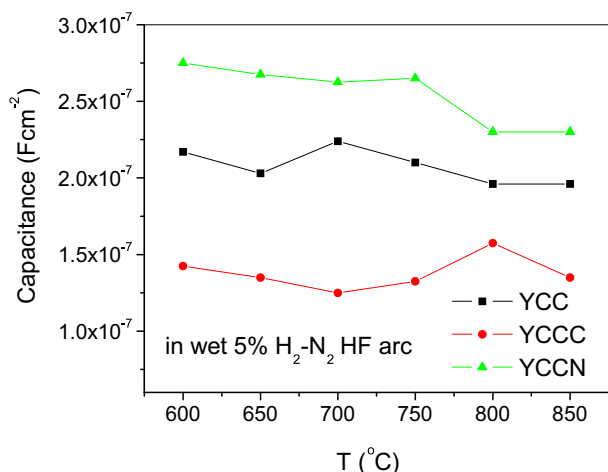


Fig. 7. Capacitance of HF arcs for YCCs in wet 5% $\text{H}_2\text{-N}_2$.

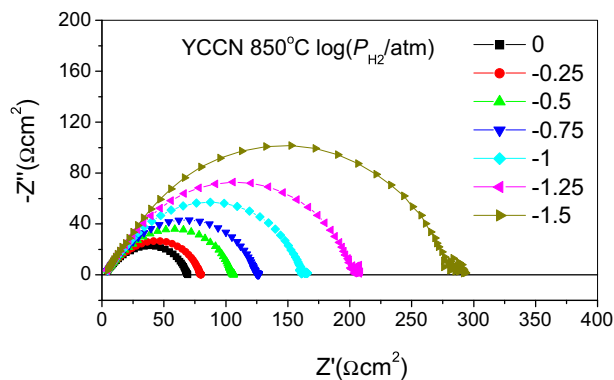


Fig. 8. Impedance of YCCN in wet $\text{H}_2\text{-N}_2$ with various H_2 content under open circuit condition at 850 °C.

- EIS in wet 5% $\text{H}_2\text{-N}_2$ consists of HF and LF arcs for the 15- μm electrode samples. E_a for HF arcs of all samples is the same regardless of composition.
- EIS from 40- μm electrode YCCN sample differ from the 15- μm one. But for the HF arc part, they have virtually the same E_a , f_0 and C.
- The resistance of HF arc for YCCN sample increased with decreasing H_2 content. The reaction order n increase from 1/3 to 1/2 as temperature rises.

4. Discussion

4.1. Enhancement of performance by doping

The HF arc from 40- μm YCCN sample operated in various P_{H_2} in Fig. 8 is associated with the same electrode process as the HF arcs in the 15- μm YCCN sample in Fig. 5, since similar frequency scope, capacitance, and E_a were observed for them. After comparing the f_0 and C identified in this study to those reported in literature for SOFC electrodes [46–47], it is safe to assign the HF arc and LF arc for YCCs in wet 5% H_2 to charge transfer and hydrogen adsorption/diffusion processes, respectively.

The performance of YCC was significantly enhanced upon Ni and Co doping as shown in Fig. 5. Compared to the LF process, the improvement on the HF process is more pronounced. For this charge transfer process at HF arc, the reaction rate is controlled by E_a and the amount of available reactants. Given all YCCs show the same E_a at HF arc, the amount of available reactants on YCCN and YCCC electrode can be expected higher for the improved charge transfer reaction. Although the ionic conductivity of YCCs is not available so far,

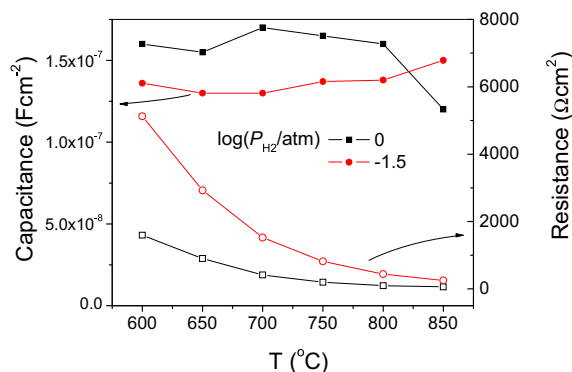


Fig. 9. R and C corresponding to HF arc from EIS of YCCN at $\log(P_{\text{H}_2}/\text{atm}) = 0$ and -1.5 .

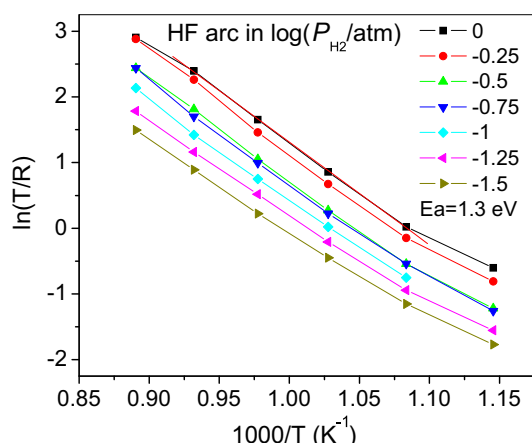


Fig. 10. Arrhenius curves for HF arc of YCCN derived from EIS in various H_2 content atmospheres.

it must possess oxygen ion conductivity in some extent especially in reducing atmosphere [15]. The oxygen non-stoichiometry of YCC was reported to be 0.06 under 10^{-18} atm P_{O_2} at 1000°C [14]. The doping of Ni and Co should further increase such value for the fact that perovskite oxides with Ni or Co as B site anion are much easier to reduce than those with Cr at B site [48]. Therefore, YCCs can be viewed as mixed ionic and electronic conductor (MIEC) in anode atmosphere. In this case, the electrode reaction can take place not only at 3PB but also at the surface of YCCs grains. In the studies of catalysis of perovskite oxides towards the oxidation of CO, CH_4 , etc. [48,49], reducibility of such materials is indicative of catalytic activity. By comparing the activity of perovskite oxides ($LaBO_3$, $B = V, Cr, Mn, Fe, Co, Ni$) at $200\text{--}850^\circ\text{C}$ for CO oxidation to for hydrocarbons oxidation, it was suggested that the activation of oxygen is probably more important than substances to be oxidized [50]. Correspondingly, certain catalytic properties of perovskite found in CO or CH_4 oxidation may be applicable to the oxidation of H_2 , especially the part from activation of lattice oxygen. The reducibility introduced by Ni and Co doping make it easier to activate lattice O in YCCs to react with H adsorbed on grain surface. The higher ionic conductivity of YCCC and YCCN would also make the supply of O from YSZ faster. Both factors above would accelerate the charge transfer reaction in 2PB where the gas channel and MIEC meet. The high activation energy (1.2–1.3 eV) found for HF in Fig. 6 could be indicative of the involvement of lattice O as well. From the viewpoint of reactant H, the coverage of adsorbed H may be enlarged by doping. In the LF arc, YCCN displayed the best performance. E_a for

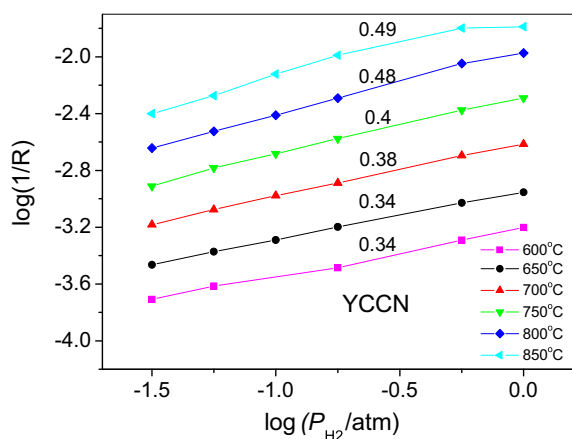


Fig. 11. H_2 dependence of HF arc for YCCN in different temperatures.

YCC, YCCC, YCCN is 1.2, 1.0, 0.5 eV, respectively, which implies the adsorption/diffusion process is thermodynamically more favorable on YCCN sample. High sticking coefficient of metal Ni for H adsorption has been reported by Morgensen et al. [20]. Good H adsorption/diffusion capability of Ni anode in SOFC is also well-known. Based on this similarity, there might be some correlation between YCCN and metal Ni at this point.

Caution must be taken when comparing the improvement of performance upon Ni doping with Co doping. The amount of physical reactive sites should be different in YCCC and YCCN. Given YCCN particle is finer the number of 3PB sites in YCCN–YSZ anode would be greater than that in YCCC–YSZ anode. And the doping level is also different. A 10% Ni doping is adopted in this study because Ni evolved from YCCN with 20% doping level when undergoing reducing atmosphere [51].

4.2. Effect of H_2 partial pressure

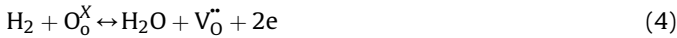
The HF arc of YCCN demonstrates a $1/3\text{--}1/2$ reaction order towards P_{H_2} as shown in Fig. 11. Results on partial pressure dependence have been extensively reported in literature for Ni/YSZ system [46,47,52–55]. Jiang reported the HF arc for Ni/YSZ electrode decreased when H_2 content in $H_2\text{--}N_2$ (with constant 2% H_2O) mixture decreased from 98% to 10% [47]. It is suggested more O–Ni bond or sub-oxide at Ni surface stemmed from higher P_{O_2} facilitated dissociative adsorption and diffusion of H from electrode to YSZ surface near 3PB, which in turn elevated the rate of charge transfer at 3PB. Brown et al. found resistances for high frequency arc were complicatedly dependant with P_{H_2} [22,46]. Reaction order of this arc towards P_{H_2} varied from -0.15 to 0.15 at constant H_2O content when different configurations of Ni/YSZ anode were used. In addition, for the Ni film anodes used by Nakagawa [55], HF arc exhibited no H_2 dependence in the P_{H_2} range from 10^{-2} to 1 with constant 2% H_2O . However, none of the observations in Ni/YSZ system can be easily applied to interpret the kinetic behavior of ceramic anodes and there have been very few studies on H_2 oxidation mechanism in ceramic anodes in SOFC. In the studies of catalytic activity of anode material by Rossmeisl and Setoguchi [56,57], it was concluded that for a desirable anode catalyst, the strength of oxygen-metal bond should be strong enough to get oxygen from electrolyte and weak enough to avoid poisoning the catalyst surface. Of all the metals investigated, Ni showed medium bind energy with O, resulting in the highest catalytic activity. From this point of view, the intermediate binding energy between Ni and O might be the key for the O–Ni species to work out. In contrast, perovskite oxides with Cr at B site display poor O adsorption according to kinetics of O_2 adsorption and non-stoichiometric surface behavior studies [58,59]. Therefore it is difficult for YCCs to hold O stably on the surface especially in an extremely reducing atmosphere. In addition, relatively high surface H coverage is demanded in spillover effect. Otherwise the supply of H would be mitigated by lowering P_{H_2} . Although surface H coverage of YCCs is unknown, one can assume reasonably that it should be lower than that of metal Ni.

On the other hand, it seems comprehensible that higher concentration of reactant (H_2) gives rise to larger exchange current and consequently smaller resistance. However, the adsorbed H but not H_2 molecule is involved directly into charger transfer process in HF arc. According to observation by Mogensen and Skaarup [20]. The sticking coefficient of H on Ni increases with temperature, and was about 0.3 at SOFC operating temperature even for the most unfavorable crystal face, rendering a high H coverage on Ni surface. If the coverage of adsorbed H on electrode surface is high enough, such process would not be affected by H_2 molecule content. This is in agreement with the results from the Ni film anodes by Nakagawa and coarse Ni/YSZ cermet by Brown as mentioned above, where the

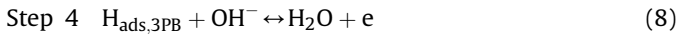
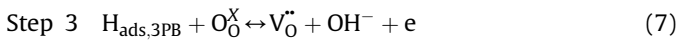
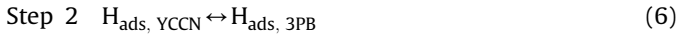
HF arcs were insensitive to P_{H_2} . Nonetheless, with lower H coverage, the performance of YCCN would be harmed by limitation of H supply when decreasing P_{H_2} . In addition, both the ionic conductivity and activation of lattice oxygen are closely related to the content of H_2 , which play important roles in the charge transfer step as discussed above. Hence, it is not surprising that YCCN showed H_2 dependence in opposite to the Ni/YSZ anode.

4.3. Possible H_2 oxidation mechanisms

The overall H_2 oxidation reaction in anode can be represented in Eq. (4),



Several steps must occur before H_2 is thoroughly oxidized as above. Base on the observed results, one possible model for the reaction path on YCCs anodes in this paper can be presented as following:



After the following assumptions are taken, like the LaMnO₃ cathode study by Heuveln and Bouwmeester [60]: 1) these reactions are microscopic reversible; 2) adsorption of any species is governed by Langmuir type isotherm; 3) the surface coverage for all adsorbed species is low, the corresponding rate equations can be written as:

$$r_1 = k_1 P_{H_2} - k_1^- a_{H_{\text{ads}}}^2 \quad (9)$$

$$r_2 = k_2 a_{H_{\text{ads}}} - k_2^- a_{H_{3PB}} \quad (10)$$

$$r_3 = k_3 a_{H_{3PB}} \exp(\beta fE) - k_3^- a_{OH_{3PB}} \exp(-\alpha fE) \quad (11)$$

$$r_4 = k_4 a_{H_{3PB}} a_{OH_{3PB}} \exp(\beta fE) - k_4^- P_{H_2O} \exp(-\alpha fE) \quad (12)$$

where k_i and k_i^- are the rate constant for the corresponding anodic and cathodic reaction; $f = F/RT$ (F , R and T have their usual physical meaning) and E the electrode potential. α and β are symmetric coefficients. The activity of lattice oxygen and oxygen vacancy is taken as constant regardless of the change of P_{H_2} . This assumption doesn't directly reflect the improvement effects from Ni/Co doping on lattice oxygen activation and oxygen vacancy concentration discussed above in Section 4.1. If the 3PB vacancy concentration is increased by Ni/Co doping, higher exchange current density for the rate-limiting step (rds) would be expected but this should not change kinetic scenario of P_{H_2} dependence.

Given the resistance from charge transfer corresponding to HF arc is greatest in most cases as shown in Figs. 5 and 8, we first assume the charge transfer step (step 3) is the rds and the other steps are in near equilibrium. It follows:

$$a_{H_{\text{ads}}} = \sqrt{\frac{k_1 P_{H_2}}{k_1^-}} \quad (13)$$

$$a_{H_{3PB}} = \frac{k_2 a_{H_{\text{ads}}}}{k_2^-} \quad (14)$$

$$a_{OH_{3PB}} = \frac{k_4^- P_{H_2O}}{k_4 a_{H_{3PB}} \exp(fE)} \quad (15)$$

Substituting of Eqs. (13)–(15) to Eq. (11), it follows:

$$r_3 = k_3 \frac{k_4^- k_2}{k_4 k_2^-} \sqrt{\frac{k_1 P_{H_2}}{k_1^-}} \exp(\beta fE) - k_3^- \frac{k_4^- k_2 P_{H_2O}}{k_4 k_2^-} \sqrt{\frac{k_1^-}{k_1 P_{H_2}}} \exp(-(1+\alpha)fE) \quad (16)$$

Eq. (16) indicates the steady state reaction rate of step 3, which can be converted to current density using the relationship of $i = nFr$. In equilibrium condition there is no net current, i.e. $r_3 = 0$, it reveals the Nernst potential:

$$E = \text{const} + \frac{RT}{2F} \ln \frac{P_{H_2O}}{P_{H_2}} \quad (17)$$

Inserting Eq. (17) back into Eq. (16) yields the relationship of $i_{0,3} \propto P_{H_2}^{1/4}$ (take $\alpha = \beta = 0.5$). P_{H_2O} at OCV is almost fixed, 0.03 atm, in the present experiment. Similarly, if assuming the second charge transfer step (step 4) the rds, $i_{0,4} \propto P_{H_2}^{1/4}$ can be drawn also. Thus, a 1/4 reaction order is predicted at high frequency domain.

Beside the YCCN sample, an YCCC sample was also tested at five atmospheres with various H_2 content from $10^{-1.5}$ to 1 atm in the similar routine used in the YCCN case. Fig. 12 demonstrates the H_2 dependence of HF arc for YCCC. The reaction orders are around 1/4, in accordance with predicted by this model.

It should be pointed out that the agreement found for interpretation of experimental observance with the modeled reaction scenario does not exclude other reaction mechanisms for YCCs. As discussed above, doped YCCs possess some level of ionic conductivity at very low P_{H_2} condition. They turn MIEC when working as anodes, and the charge transfer process (step 3 and 4) not only take place at 3PB area but also occur at 2PB area as O ions can be transported through the bulk of YCCs. The activity of oxygen vacancy in step 3 for 2PB reaction is no longer constant, but dependent to P_{H_2} . Also the influence of electron transportation on reaction rate in these charge transfer steps is neglected in this model. While it could be fair to ignore such factor for the high electronic conductivity electrode materials, like Ni in anode or LSM in cathode, the influence of electrons transportation in YCCs anodes

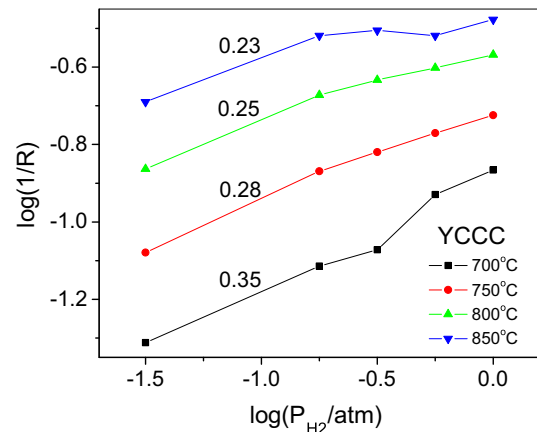


Fig. 12. H_2 dependence of HF arc for YCCC in different temperatures.

might not be negligible since the electronic conductivity of such materials are much lower and affected by P_{H_2} [11, 17]. What's more, besides H adsorption, O and H_2O can be adsorbed on electrode surface as well, leading to a complex competitive adsorption model as studies by Ihara and Mizusaki [26,61]. Given all these issues above, the reaction path in anode may be more complicated than that in this model, and the H_2 dependence would be more intricate than derived in this study as well.

However, to further justify this model and verify the dominant reaction mechanism, more experiments are needed, such as EIS study under polarization condition, the effect of H_2O on polarization resistance and etc., which are the subjects of upcoming investigation.

5. Conclusions

In this study, doped YCCs as potential anode materials were made and investigated by EIS. The effect of doping on electrode performance was discussed. A possible anode reaction model was proposed based on the results of H_2 dependence testing.

It was found that two electrode processes, featured at HF and LF arcs, could dominate the spectra. Charge transfer and surface adsorption/diffusion processes were respectively identified as the corresponding reactions in the HF and LF arcs. The polarization resistance of YCC was significantly decreased upon Ni and Co doping. Ni doping facilitated surface process at LF domain by decreasing the corresponding activation energy, and improved the charge transfer process probably by enlarging the surface coverage of adsorbed H. In H_2 dependence testing, the reaction order of HF arc was 1/4 for YCCC, 1/3–1/2 for YCCN. The proposed model in this study suggested such dependence originated from the reaction between adsorbed H and the lattice oxygen.

Acknowledgements

This work is sponsored by US Department of Energy EPSCoR Program under grant number DE-FG02-06ER46299. Dr. Tim Fitzsimmons is the DOE Technical Monitor. Dr. Richard Bajura is the Administrative Manager and Dr. Ismail Celik is the Technical Manager and Principal Investigator of WVU EPSCoR project.

References

- [1] M. Gong, X. Liu, J. Tremblay, C. Johnson, J. Power Sources 168 (2007) 289–298.
- [2] S. Tao, J.T.S. Irvine, J. Electrochem. Soc. 151 (2004) A252–A259.
- [3] G. Kim, S. Lee, J. Shin, G. Corre, J. Irvine, J. Vohs, R.J. Gorte, Electrochem. Solid-State Lett. 12 (2009) B48–B52.
- [4] S. Tao, J.T.S. Irvine, Nat. Mater. 2 (2003) 320–323.
- [5] D.M. Bastidas, S. Tao, J.T.S. Irvine, J. Mater. Chem. 16 (2006) 1603–1605.
- [6] J. Canales-Vázquez, S.W. Tao, J.T.S. Irvine, Solid State Ionics 159 (2003) 159–165.
- [7] O.A. Marina, N.L. Canfield, J.W. Stevenson, Solid State Ionics 149 (2002) 21–28.
- [8] S. Hashimoto, L. Kindermann, F.W. Poulsen, M. Mogensen, J. Alloys Compd. 397 (2005) 245–249.
- [9] Q.X. Fu, F. Tietz, D. Stöver, J. Electrochem. Soc. 153 (2006) D74–D83.
- [10] R. Voorhoeve, D. Johnson, J. Remeika, P. Gallagher, Science 195 (1977) 827–833.
- [11] K.J. Yoon, J.W. Stevenson, O.A. Marina, J. Power Sources 196 (2011) 8531–8538.
- [12] S. Wang, B. Lin, Y. Dong, D. Fang, H. Ding, X. Liu, G. Meng, J. Power Sources 188 (2009) 483–488.
- [13] K.J. Yoon, C.N. Cramer, E.C. Thomsen, C.A. Coyle, G.W. Coffey, O.A. Marina, J. Electrochem. Soc. 157 (2010) B856–B861.
- [14] T.R. Armstrong, J.W. Stevenson, D.E. McCready, S.W. Paulik, P.E. Raney, Solid State Ionics 92 (1996) 213–223.
- [15] G. Carini, H. Anderson, D. Sparlin, M. Nasrallah, Solid State Ionics 49 (1991) 233–243.
- [16] W.J. Weber, C.W. Griffin, J.L. Bates, J. Am. Ceram. Soc. 70 (1987) 265–270.
- [17] K.J. Yoon, J.W. Stevenson, O.A. Marina, Solid State Ionics 193 (2011) 60–65.
- [18] K.J. Yoon, C.A. Coyle, O.A. Marina, Electrochem. Commun. 13 (2011) 1400–1403.
- [19] T. Horita, H. Kishimoto, K. Yamaji, Y. Xiong, N. Sakai, M.E. Brito, H. Yokokawa, Solid State Ionics 177 (2006) 1941–1948.
- [20] M. Mogensen, S. Skaarup, Solid State Ionics 86 (1996) 1151–1160.
- [21] P. Holtappels, I. Vinke, L. De Haart, U. Stimming, J. Electrochem. Soc. 146 (1999) 2976–2982.
- [22] S. Primdahl, M. Mogensen, J. Electrochem. Soc. 144 (1997) 3409–3419.
- [23] S. Jiang, Y. Ramprakash, Solid State Ionics 122 (1999) 211–222.
- [24] J. Mizusaki, K. Amano, S. Yamauchi, K. Fueki, Solid State Ionics 22 (1987) 323–330.
- [25] J. Mizusaki, H. Tagawa, T. Saito, T. Yamamura, K. Kamitani, K. Hirano, S. Ehara, T. Takagi, T. Hikita, M. Ippommatsu, Solid State Ionics 70 (1994) 52–58.
- [26] M. Ihara, T. Kusano, C. Yokoyama, J. Electrochem. Soc. 148 (2001) A209–A219.
- [27] S. Primdahl, M. Mogensen, Solid State Ionics 152 (2002) 597–608.
- [28] A. Bieberle, L. Gauckler, Solid State Ionics 135 (2000) 337–345.
- [29] S.H. Jensen, A. Hauch, P.V. Hendriksen, M. Mogensen, N. Bonanos, T. Jacobsen, J. Electrochem. Soc. 154 (2007) B1325–B1330.
- [30] Q.A. Huang, R. Hui, B. Wang, J. Zhang, Electrochim. Acta 52 (2007) 8144–8164.
- [31] J.D. Kim, G.D. Kim, J.W. Moon, Y. Park, W.H. Lee, K. Kobayashi, M. Nagai, C.E. Kim, Solid State Ionics 143 (2001) 379–389.
- [32] X. Ding, Y. Liu, L. Gao, L. Guo, J. Alloys Compd. 458 (2008) 346–350.
- [33] Z. Shao, W. Zhou, Z. Zhu, Prog. Mater. Sci. 57 (2012) 804–874.
- [34] O. Demircan, C. Xu, J. Zondlo, H.O. Finklea, J. Power Sources 194 (2009) 214–219.
- [35] L. Van der Pauw, Philips Tech. Rev. 20 (1958) 220–224.
- [36] L.A. Chick, J. Liu, J.W. Stevenson, T.R. Armstrong, D.E. McCready, G.D. Maupin, G.W. Coffey, C.A. Coyle, J. Am. Ceram. Soc. 80 (1997) 2109–2120.
- [37] J. Carter, C. Appel, M. Mogensen, J. Solid State Chem. 122 (1996) 407–415.
- [38] A. Kaiser, B. Sommer, E. Woermann, J. Am. Ceram. Soc. 75 (1992) 1463–1471.
- [39] N. Sakai, T. Kawada, H. Yokokawa, M. Dokiya, I. Kojima, J. Am. Ceram. Soc. 76 (1993) 609–616.
- [40] R. Koc, H.U. Anderson, J. Eur. Ceram. Soc. 9 (1992) 285–292.
- [41] H. Juretschke, R. Landauer, J. Swanson, J. Appl. Phys. 27 (1956) 838–839.
- [42] W. Scheider, J. Phys. Chem. 79 (1975) 127–136.
- [43] T. Jacobsen, B. Zachau-Christiansen, L. Bay, S. Skaarup, in: Proceedings of the 17th Riso International Symposium on Materials Science, vol. 29–40, 1996.
- [44] G. Brug, A. Van Den Eeden, M. Sluyters-Rehbach, J. Sluyters, J. Electroanal. Chem. Interf. Electrochem. 176 (1984) 275–295.
- [45] M.J. Jørgensen, M. Mogensen, J. Electrochem. Soc. 148 (2001) A433–A442.
- [46] M. Brown, S. Primdahl, M. Mogensen, J. Electrochem. Soc. 147 (2000) 475–485.
- [47] S.P. Jiang, S.P.S. Badwal, Solid State Ionics 123 (1999) 209–224.
- [48] J. Fierro, J. Tascon, L.G. Tejuca, J. Catal. 93 (1985) 83–91.
- [49] H. Arai, T. Yamada, K. Eguchi, T. Seiyama, Appl. Catal. 26 (1986) 265–276.
- [50] N. Yamazoe, Y. Teraoka, Catal. Today 8 (1990) 175–199.
- [51] K.J. Yoon, C.N. Cramer, J.W. Stevenson, O.A. Marina, J. Power Sources 195 (2010) 7587–7593.
- [52] J. Mizusaki, H. Tagawa, T. Saito, K. Kamitani, T. Yamamura, K. Hirano, S. Ehara, T. Takagi, T. Hikita, M. Ippommatsu, S. Nakagawa, K. Hashimoto, J. Electrochem. Soc. 141 (1994) 2129–2134.
- [53] J. Mizusaki, H. Tagawa, T. Saito, T. Yamamura, K. Kamitani, K. Hirano, S. Ehara, T. Takagi, T. Hikita, M. Ippommatsu, S. Nakagawa, K. Hashimoto, Solid State Ionics 70–71 (1994) 52–58.
- [54] S. Jiang, S. Badwal, J. Electrochem. Soc. 144 (1997) 3777–3784.
- [55] N. Nakagawa, H. Sakurai, K. Kondo, T. Morimoto, K. Hatanaka, K. Kato, J. Electrochem. Soc. 142 (1995) 3474–3479.
- [56] J. Rossmeisl, W.G. Bessler, Solid State Ionics 178 (2008) 1694–1700.
- [57] T. Setoguchi, K. Okamoto, K. Eguchi, H. Arai, J. Electrochem. Soc. 139 (1992) 2875–2880.
- [58] J. Fierro, L.G. Tejuca, Appl. Surf. Sci. 27 (1987) 453–457.
- [59] J. Fierro, L.G. Tejuca, J. Catal. 87 (1984) 126–135.
- [60] F.H. Heuveln, H. Bouwmeester, J. Electrochem. Soc. 144 (1997) 134–140.
- [61] J. Mizusaki, H. Tagawa, K. Isobe, M. Tajika, I. Koshiro, H. Maruyama, K. Hirano, J. Electrochem. Soc. 141 (1994) 1674.